Letter Editors' Suggestion

Quantum Wigner molecules in moiré materials

Constantine Yannouleas [*] and Uzi Landman [†]

School of Physics, Georgia Institute of Technology, Atlanta, Georgia 30332-0430, USA

The few-body problem (with $N \leqslant 6$ fermionic charge carriers) in isolated moiré quantum dots (MQDs) in transition metal dichalcogenide (TMD) bilayer materials with integer fillings, $\nu \geqslant 2$, is investigated by employing large-scale full configuration interaction (FCI; also termed exact diagonalization) computations, and by performing a comparative analysis of the ensuing first-order (charge densities) and second-order (conditional probability distributions, CPDs) correlation functions. With parameters representative of bilayer experimental TMD setups, our investigations reveal the determining role of the strong interparticle Coulombic repulsion in bringing about Wigner molecularization, which is associated with many-body physics beyond both that described by the Aufbau principle of natural atoms, as well as by the widely used Hubbard model for strongly interacting condensed-matter systems. In particular, for weak and moderate trilobal crystal-field deformations of the MQDs, the imperative employment of the CPDs brings to light the geometrical polygonal-ring configurations underlying the Wigner molecules (WMs) that remain hidden at the level of a charge-density analysis, apart from the case of $N = 3$ when a *pinned* WM emerges in the charge density due to the coincidence of the C_3 symmetries associated with both the intrinsic geometry of the $N = 3$ WM and the TMD trilobal crystal field of the confining pocket potential. The FCI numerically exact diagonalization results provide critical benchmarks for assessing and guiding the development of future computational methodologies of interacting strongly correlated fermions in isolated MQDs and their superlattices in TMD materials.

Understanding of the electronic spectral and configurational organization in natural atoms, which played a pivotal role in the early development of quantum mechanics [1,2], continues to inspire discoveries in research targeting the exploration of the nature of a few charged carriers trapped in artificially fabricated, isolated or superlattice-assembled, quantum dots (QDs) [3–5]. Such research aims at utilizing these systems, with high tunability and control, in future quantum information and computational platforms [6–9]. Earlier studies have unveiled formation of quantum Wigner molecules (WMs), originally predicted theoretically [10–33] in two-dimensional (2D) semiconductor QDs, as well as in trapped ultracold atoms, and subsequently observed experimentally in GaAs QDs [34–37], Si/SiGe QDs [38], and carbon nanotubes [39]. Important contributions to this area employed full configuration-interaction (FCI) [17,18,22,24,28,29,33,40–44] calculations, going beyond (1) the central-field Aufbau principle, which underlies the periodic table of natural atoms [45], and (2) the Hubbard modeling of strongly interacting systems [46,47].

Here we broaden the above WM portfolio, by uncovering, with the use of FCI calculations, the ubiquitous formation of WMs in a novel class of two-dimensional (2D) materials which emerged recently as a most promising platform for investigations of strongly correlated electrons. These materials form moiré superlattices (with large, tunable lattice constants)

when 2D crystals (made of semiconductor or semimetal materials) are stacked with a small twist angle or lattice mismatch; for references to the developing literature on twisted Γ-valley homo-bilayer (e.g., MoS$_2$) or hetero-bilayer (e.g., WSe$_2$/WS$_2$, MoSe$_2$/WSe$_2$) transition metal dichalcogenides (TMDs), and the emergent twistronics field, see [48–52].

We focus here on few-fermion ($N < 7$, electrons or holes) moiré quantum dots (MQDs) [53–55] formed at the upper layer of doped integer-filled bilayer TMDs [56,57]. The potential confining these fermions at the minima of the 2D moiré superlattice can be approximated by the expression [50–52]

$$V(\mathbf{r}) = -2v_0 \sum_{i=1}^{3} \cos(\mathbf{G}_i \cdot \mathbf{r} + \phi), \qquad (1)$$

where $\mathbf{G}_i = [(4\pi/\sqrt{3}a_M)(\sin(2\pi i/3), \cos(2\pi i/3))]$ are the moiré reciprocal lattice vectors. The material-specific parameters of $V(\mathbf{r})$ are v_0 (which can also be experimentally controlled through voltage biasing), the moiré lattice constant a_M, and the angle ϕ; for variations of $V(\mathbf{r})$ with ϕ, see Fig. 1; a_M is typically of the order of 10 nm, which is much larger than the lattice constant of the monolayer TMD material (typically a few Å). The parameter ϕ controls the strength of the trilobal crystal-field-type anisotropy in each MQD potential pocket.

For angles $\phi < 40°$ and a large ratio $v_0/E_K \gg 1$, where the moiré kinetic energy $E_K = \hbar^2/(2m^* a_M^2)$ [51], with m^* being the effective mass of the charge carriers (referred to here, indiscriminately, as "holes"), the attractive pockets of $V(\mathbf{r})$ represent a periodic array of isolated MQDs [53–55],

*Constantine.Yannouleas@physics.gatech.edu
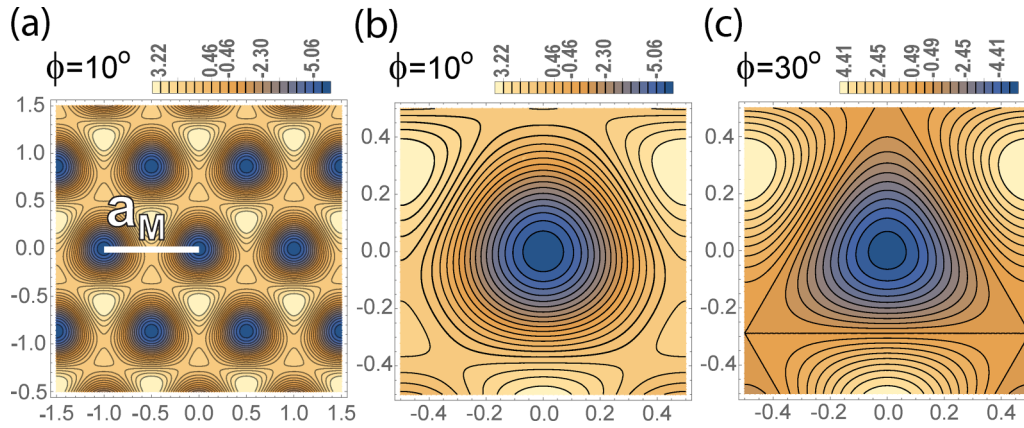†Uzi.Landman@physics.gatech.edu

FIG. 1. Plot of the moiré-superlattice potential given by Eq. (1). (a) Broader view of the periodic potential structure for an angle of $\phi = 10°$. (b) Potential of the isolated moiré QD for $\phi = 10°$. (c) Potential of the isolated moiré QD for $\phi = 30°$. Lengths in units of the moiré lattice constant a_M. Potential contours in units of v_0. Note the change of the length scale in (b) and (c) compared to (a).

where the carriers are tightly bound. In a superlattice with integer fillings, the corresponding strongly interacting few-body problem (with $N \leqslant 6$ holes) has already been experimentally realized [56,57].

A prerequisite to materialization of gate-controlled tunable MQDs in bilayer TMDs (in isolation or in superlattices) with integer fillings (via doping) in quantum information and simulations is a thorough understanding of the correlated electronic states of the strongly interacting MQD-confined charge carriers. To this aim we concentrate on TMD materials with a large lattice constant, a_M, where the MQDs are evocative of the electrostatically defined ones in 2D semiconductors (SQDs; e.g., in GaAs [22]) with a major difference which is readily grasped by expanding $V(\mathbf{r})$ in Eq. (1) in powers of r, and defining a confining potential, $V_{\mathrm{MQD}}(\mathbf{r})$, for the isolated MQD as follows:

$$V_{\mathrm{MQD}}(\mathbf{r}) \equiv V(\mathbf{r}) + 6v_0 \cos(\phi) \approx m^* \omega_0^2 r^2/2 + \mathcal{C}\sin(3\theta)r^3,$$

$$(2)$$

with $m^* = 0.50m_e$, $m^*\omega_0^2 = 16\pi^2 v_0 \cos(\phi)/a_M^2$, and $\mathcal{C} = 16\pi^3 v_0 \sin(\phi)/(3\sqrt{3}a_M^3)$ [the expansion of $V(\mathbf{r})$ can be restricted to the terms up to r^3]. Because of the anisotropic second term, the $V_{\mathrm{MQD}}(\mathbf{r})$ confinement [Eq. (2)] has a crystal-field, C_3 (trilobal) point-group symmetry and differs from that of the extensively studied single circular 2D QD, which is well approximated solely by the harmonic term [first term in $V_{\mathrm{MQD}}(\mathbf{r})$ above]. Furthermore, consideration of anisotropic confinements in SQDs have treated elliptic-in-shape distortions [using $\omega_{0x} \neq \omega_{0y}$ in place of a single ω_0 and $\mathcal{C} = 0$ in Eq. (2)], under the influence of applied magnetic fields, B [22,31,58,59], lacking a comprehensive study of the trilobal anisotropy in QDs for $B = 0$ (the case of the MQD where diamagnetic effects are negligible due to large values of $\hbar\omega_0$).

Below, we analyze (using representative materials' parameters corresponding to experimentally investigated and theoretically modeled TMD materials [50,51,54,57]) the emergence of quantum moiré WMs (MWMs) in the above trilobal confinement. Specifically, our FCI results will show that a relatively weak $\sin(3\theta)r^3$ term (the case of $\phi < 15°$) can act as a pinning agent for the WM only in the case

of $N = 3$, when the intrinsic WM azimuthal geometry [an empty-center (0,3) polygonal ring] coincides with the C_3 point-group symmetry associated with $\sin(3\theta)$; in this pinned case, the WM is visible in the charge density. In all other instances investigated here, however, there is no pinning [60]; i.e., while the charge densities (CDs) preserve the C_3 symmetry (as quantum-mechanically required), they do not exhibit any signature of Wigner molecularization. Unveiling (seeing) the hidden (unseen) Wigner molecularization necessitates analysis which reaches beyond the information given by the CD distribution in the MQD; that is, it requires analysis of spin-resolved density-density or conditional probability distributions (CPDs; see, e.g., Refs. [12,19,21,22,28,61]; for the definition, see the Supplemental Material (SM) [62]), which reveal the intrinsic (n_1, n_2) (with $n_1 + n_2 = N$, $N = 2$–6) concentric polygonal-ring configurations, familiar from the literature [10,12,14,15,17–19,21–23,25,26,32,33] on circular SQDs.

The Schrödinger equation for the many-body Hamiltonian of the isolated moiré QD, given by

$$H_{\mathrm{MB}} = \sum_{i=1}^{N} \left\{ \frac{\mathbf{p}_i^2}{2m^*} + V_{\mathrm{MQD}}(\mathbf{r}_i) \right\} + \sum_{i<j}^{N} \frac{e^2}{\kappa|\mathbf{r}_i - \mathbf{r}_j|}, \quad (3)$$

is solved here using the FCI methodology [17,18,22,33,40,42–44]; for a brief description of this methodology, see the SM [62], including Ref. [63]. The emergence of MWMs is analyzed using both the FCI CDs and CPDs. κ is the effective dielectric constant obtained as the geometric mean of the anisotropic in-plane and perpendicular tensor components of the MQD TMD dielectric environment (most often [50,54,57] hexagonal boron nitride, hBN, when $\kappa \approx 5$). We remark that because the spin and valley degrees of freedom are locked for the holes in TMD materials [50,51,64,65] only the spin needs to be considered in the course of the FCI exact diagonalization of H_{MB}.

For values of $\phi = 10°$ and $\phi = 30°$, $V_{\mathrm{MQD}}(\mathbf{r})$ exhibits, respectively, weak and strong $\sin(3\theta)r^3$ distortions away from the circular confinement ($\phi = 0$); see illustration in Fig. 1. In Figs. 2 and 3, we analyze primarily the $\phi = 10°$ case, with an exception for $\phi = 30°$ in Fig. 2(d). Additional results

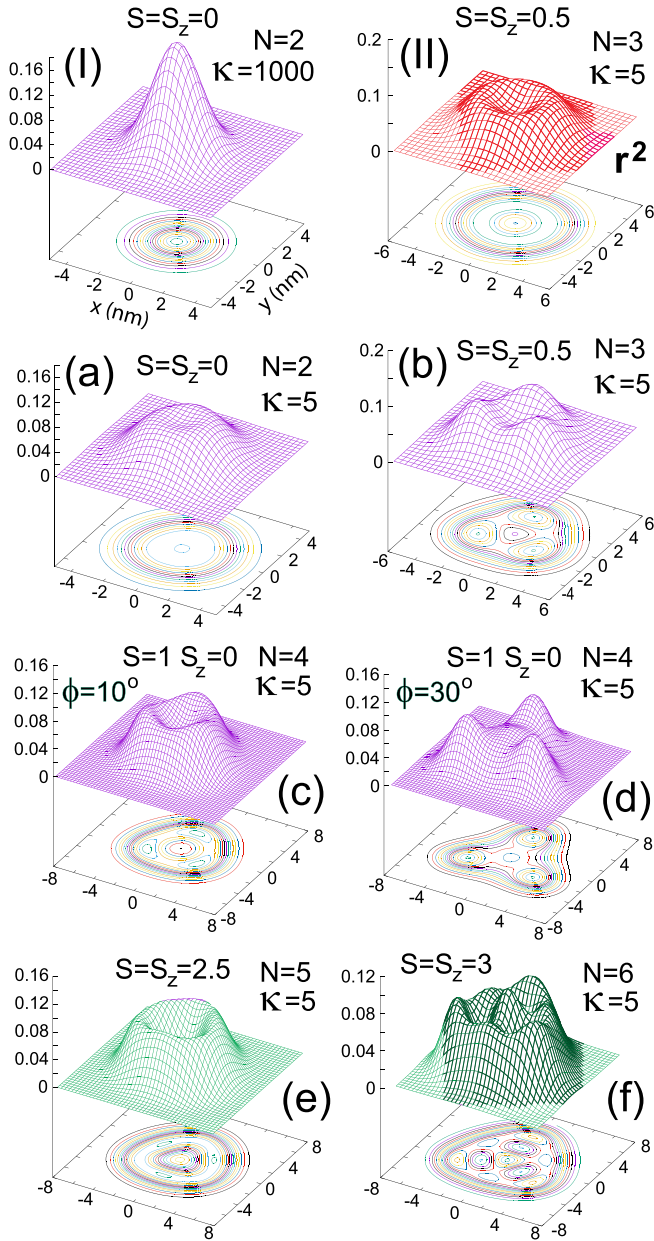FIG. 2. FCI CDs (normalized to N) for $N = 2$–6 holes in the isolated MQD. In all frames: $a_M = 14$ nm, $m^* = 0.5m_e$, $\phi = 10°$, $v_0 = 15$ meV, resulting in $\hbar\omega_0 = 42.59073$ meV [but $\phi = 30°$ in (d)]. $\kappa = 5.0$ ($R_W = 3.57$) except in frame (I), where $\kappa = 1000$ ($R_W = 0.018$) mimics the noninteracting limit. In all cases, the total anisotropic confinement was considered, except in frame (II) (red-colored surface) where the confinement consists solely of the 2D circular harmonic contribution. The green color denotes fully polarized ($S = S_z = N/2$) cases. A vanishing magnetic field, $B = 0$, was considered, except for $N = 3$ and $N = 5$ where a value of $B = 1$ T was used in order to simply lift the ground-state degeneracy. Frames for non-fully-polarized cases describe low-spin ground states. CDs in units of $1/\text{nm}^2$. See the text for a full description.

FIG. 3. FCI spin-resolved CPDs (normalized to unity) for $N = 2$–6 holes in the isolated MQD. Parameters as denoted (compare Fig. 2). $a_M = 14$ nm, $m^* = 0.5m_e$, $\phi = 10°$, $v_0 = 15$ meV. In all cases, the total anisotropic $V_{\text{MQD}}(\mathbf{r})$ was considered, except in (b) (red-colored surface) where the confinement consists solely of the 2D circular harmonic contribution. The green color denotes again fully polarized ($S = S_z = N/2$) cases, and all the remaining frames describe low-spin ground states. The black solid dot and black arrows denote the position and spin direction of the fixed-point fermions, respectively. The red arrows denote the positions (maxima of the spin surfaces) and spin direction of the remaining $N - 1$ fermions. $B = 0$, except for $N = 3$ and $N = 5$ where a value of $B = 1$ T was used in order to simply lift the ground-state degeneracy. CPDs in units of $1/\text{nm}^2$. See the text for a full description.

for $\phi = 30°$, as well as $\phi = 0$ and $\phi = 10°$, are presented in the SM [62]. The Wigner-molecularization propensity uncovered from the FCI results is controlled by the Wigner parameter $R_W = e^2/(\kappa l_0 \hbar\omega_0)$ [10,22], expressing the ratio
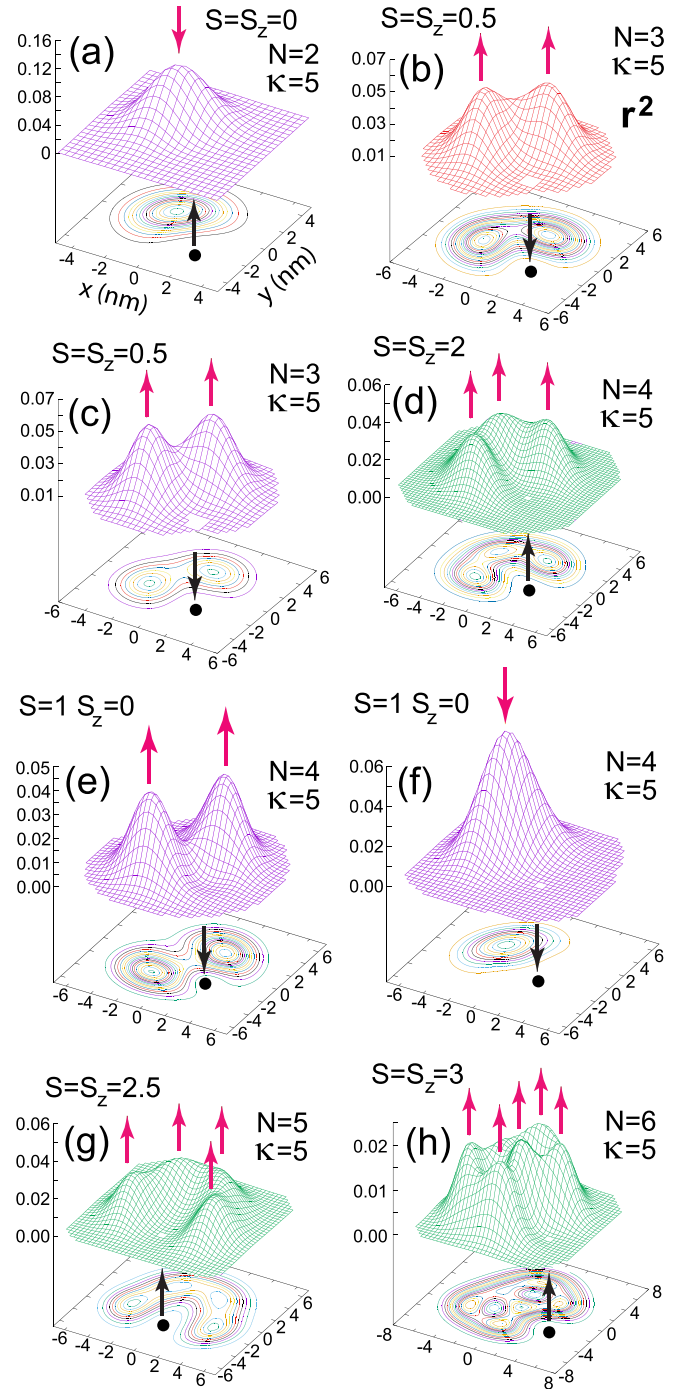
between the Coulomb repulsion and the quantum kinetic energy (proportional to the harmonic-oscillator energy gap); $l_0 = [\hbar/(m^*\omega_0)]^{1/2}$ is the oscillator length. A high Wigner molecularization propensity is expected for $R_W > 1$.

Figure 2 displays CDs for $N \leqslant 6$ in various instances for holes when $\phi = 10°$. For contrast, Fig. 2(d) employs $\phi = 30°$ and in Fig. 2(II) only the circular partial r^2 term has been employed in $V_{MQD}(\mathbf{r})$. In Fig. 2(I), $\kappa = 1000$ was used to simulate the noninteracting limit, whereas $\kappa = 5$ (strongly interacting regime appropriate for the MQD in an hBN environment) was used in the rest of the frames.

The two frames for $N = 2$ [with $S = S_z = 0$; Fig. 2(I) and Fig. 2(a)] demonstrate the effect of an increasing interparticle Coulomb repulsion (decreasing κ) on the CDs. Indeed, in Fig. 2(I) (with $\kappa = 1000$; noninteracting regime) the CD is associated with a doubly occupied $1s$ orbital. In contrast, for $\kappa = 5$ (MQD/hNB case), the $N = 2$ CD in Fig. 2(a) is spread out over a considerably larger area and it assumes a ringlike shape by developing a depression at the origin. This ringlike shape preserves the C_3 symmetry of the $V_{MQD}(\mathbf{r})$ by being slightly deformed.

The CD in Fig. 2(a) does not exhibit the anticipated azimuthal geometry of a diatomic molecule, namely two localized particles in an antipodal arrangement. This WM configuration remains hidden in the CD of Fig. 2(a), but it is revealed in the spin-resolved CPD displayed in Fig. 3(a). Indeed, for a spin-up fixed hole, the second hole is found in an antipodal position with an opposite spin, as is consistent for a singlet state ($S = S_z = 0$).

For $N = 3$, the CDs in Fig. 2(II) and Fig. 2(b) exhibit different behaviors. Specifically, when only the isotropic r^2 term is retained in Eq. (2), the CD is an azimuthally uniform ring [Fig. 2(II)]. However, further inclusion of the anisotropic $\sin(3\theta)r^3$ term in $V_{MQD}(\mathbf{r})$ results in a drastic change; the CD becomes that of three holes localized at the apices of an equilateral triangle [Fig. 2(b)]. One then can talk of a profoundly quantum, "rotating" (0,3) intrinsic WM polygonal-ring structure [66] in the case of Fig. 2(II), which transforms into a *pinned* WM in Fig. 2(b); the intrinsic (0,3) molecular structure is *unseen* in the CD of the isotropic confinement [Fig. 2(II)], but it becomes visible in the spin-resolved CPD in Fig. 3(b). For completeness, we also display [Fig. 3(c)] the spin-resolved CPD for $N = 3$ associated with the total potential, which is redundant, however, since, in this case, the (0,3) molecular configuration is already revealed in the CD [Fig. 2(b)].

With same parameters, the CDs for $N = 4$ (ground state), and for $N = 5$ and $N = 6$ (lowest-in-energy fully spin-polarized states) are displayed in Fig. 2(c), Fig. 2(e), and Fig. 2(f), respectively. These three densities preserve the C_3 symmetry of the external confinement, but they are similar in shape and do not reveal any intrinsic molecular structure. Again, the intrinsic (n_1, n_2) polygonal configurations are revealed through the FCI CPDs. In particular, two spin-resolved CPDs [spin-down at fixed point, look for the two spin-ups, Fig. 3(e), and spin-down at fixed point, look for the other spin-down, Fig. 3(f)], associated with the $N = 4$ ground-state density in Fig. 2(c), are presented. Taking into account the two remaining CPDs (spin-up, look for spin-up and spin-up, look for spin-down, not shown), one concludes that, in this
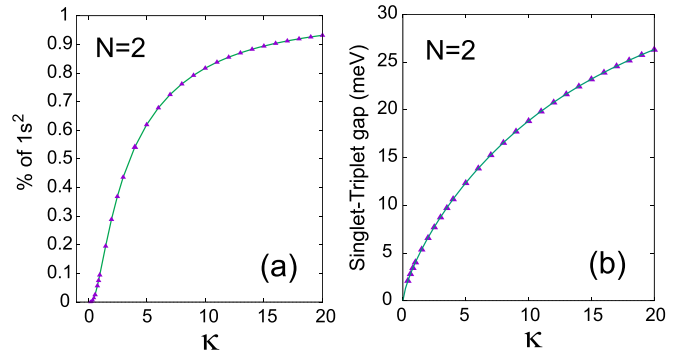

FIG. 4. (a) Weight (%) of the $1s^2$ Slater determinant [an excellent approximation of the non-interacting ground state; see Fig. 2(I)] in the FCI singlet ground state for $N = 2$, as a function of κ. (b) FCI singlet-triplet energy gap for $N = 2$ as a function of κ. Remaining parameters: $a_M = 14$ nm, $v_0 = 15$ meV, $\phi = 10°$, and $m^* = 0.5m_e$. See the text for a full description.

particular case, the intrinsic spin eigenfunction of the rotating WM has the form $(|{\uparrow}{\downarrow}{\uparrow}{\downarrow}\rangle - |{\downarrow}{\uparrow}{\downarrow}{\uparrow}\rangle)/\sqrt{2}$ [67], with the localized fermions arranged into a distorted (0,4) polygonal configuration.

In the case of the fully polarized states in Fig. 3(d) ($N = 4$), Fig. 3(g) ($N = 5$), and Fig. 3(g) ($N = 6$), there is only one spin-resolved CPD (spin-up, look for spin-up); in all three cases, this CPD reveals directly the intrinsic structure of a (0,4), (0,5), and (1,5) polygonal WM, respectively. These intrinsic polygonal configurations are necessarily slightly distorted in order to guarantee the C_3 symmetry of the charge densities; the CDs equal the integral of the CPDs over all possible positions of the fixed point [68].

Finally, the CD in Fig. 2(d) for $\phi = 30°$ illustrates that increasing the strength of the crystal-field-like trilobal anisotropy induces a structural isomeric transition [69] of the $N = 4$ MQD from a "rotating" (or gliding) (0,4) WM [Fig. 2(c)] to a pinned (1,3) one.

Using the FCI calculations for $N = 2$, we briefly discuss how the emergence of the Wigner molecularization negates the Aufbau principle that governs the natural atoms. Indeed, the ground state for the noninteracting MQD-helium is approximated by an Aufbau-type single Slater determinant denoted as $1s^2$; see Fig. 2(I). As shown in Fig. 4(a), the weight (%) of the $1s^2$ Slater determinant in the FCI wave function decreases drastically with decreasing κ (increasing correlations), and it vanishes for $\kappa \to 0$. In the CD plots, this behavior is associated with the developing of a depression at the origin (see Fig. 2(a) and Fig. SF2 in the SM [62]). For $\kappa \to 0$, singlet and triplet CDs coincide. Furthermore, in accordance, Fig. 4(b) demonstrates that the singlet-triplet energy gap [i.e., the gap Δ_{GLE} between the ground state and the lowest excited one] decreases as well with decreasing κ, and it vanishes for $\kappa \to 0$. On the contrary, because $N = 2$ is a 2D shell closure, the Aufbau approach would have yielded a value very close to the harmonic-oscillator gap, $\hbar\omega_0$ (i.e., 42.59 meV for the parameters used in Fig. 4).

The voiding of the Aufbau principle with decreasing κ (increasing R_W) can be also seen from the quenching of Δ_{GLE} for $N = 6$, which is also a closed shell in the noninteracting

limit. Indeed, for $\kappa = 3$ and the same other parameters as in Fig. 4, we find values of 1.68 meV, 2.50 meV, and 4.61 meV for the $(S = 0 \rightarrow S = 2)$, $(S = 0 \rightarrow S = 1)$, and $(S = 0 \rightarrow S = 3)$ gaps, respectively. These values are to be contrasted with the noninteracting Δ_{GLE} of $\approx \hbar\omega_0 = 42.59$ meV. This strong quenching of Δ_{GLE}'s conforms with the expected full degeneracy of Wigner crystalline states belonging to a given total-spin multiplicity in the "classical" limit $\kappa \rightarrow 0$ [70].

The FCI second differences, $\Delta_2(N) = E(N+1) + E(N-1) - 2E(N)$, associated with the ground-state energies, relate to the electrochemical potential gap $\Delta\mu$ [71], which is experimentally accessible through measurements of the bilayer-sample capacitance [56]. With respect to the TMD bilayers, the $\Delta_2(N)$ for the isolated MQD relates to capacitance measurements at integer fillings $\nu \geqslant 1$. We found the FCI values: $\Delta_2(2) = 93.55$ meV, $\Delta_2(3) = 70.73$ meV, $\Delta_2(4) = 78.06$ meV, and $\Delta_2(5) = 60.34$ meV. These values suggest two FCI trends that are in general agreement with the results of Ref. [56]: (i) Due to the Wigner molecularization, the $\Delta_2(N)$ values are substantially smaller than the corresponding Hubbard gap, $U = e^2\sqrt{\pi}/(\kappa l_0) = 269.85$ meV, and (ii) on average, $\Delta_2(N)$ decreases with increasing N [72].

Conclusions. We show that the physics of quantum WMs [10,12,14,15,17–19,21–23,25,26,32,33] underlies at integer fillings $\nu > 1$ that of TMD moiré materials, which as artificial 2D materials are fast developing into a promising experimental platform [56,57], spawning the emergence of the new field of twistronics [48–52]. Our analysis, using both FCI CDs and CPDs for the single MQD, demonstrates that the anisotropy of the moiré confinement imposes an immediately visible C_3 symmetry on the CDs, while the intrinsic polygonal-ring geometry of the WMs remains hidden and is revealed only using the CPDs. Notable exceptions are the cases of $N = 3$ (at weak) and $N = 4$ (at strong anisotropies)

charge carriers where, due to intrinsic and extrinsic symmetry coincidence, a pinned (0,3) and a pinned (1,3) WM appears in the CDs, respectively; we note here that the discrete structural features of the WMs, having a nested polygonal sliding-ring motif, can be brought to light and accentuated via pinning induced by symmetry-perturbing influences, such as QD shape-distortions (via twist, strain, or gating) or other symmetry-breaking effects [10,29,34]. Formation of the correlated MWMs results in strongly quenched energy gaps compared to those expected from both the Hubbard model and the Aufbau principle. Our FCI results provide essential benchmarks for developing future many-body computational methodologies, and in particular those based on machine learning and artificial intelligence [73]. The quantum WM phases predicted here can be experimentally verified using scanning tunneling microscopy for the CDs [53,74] and scanning probe microscopy for the CPDs [75,76].

Note added. We recently became aware of a preprint by Luo *et al.* [77] in which Wigner molecularization in isolated TMD moiré QDs has been addressed. The results reported in that work differ substantially from our benchmark FCI results. We note in particular the inability of that study, based on neural network methodology, to (1) identify formation of a Wigner molecule for $N = 2$, and (2) recover all the exact charge densities for $N > 3$. In the context of point (2) above, we call attention to pertinent remarks in Ref. [78] about ongoing issues in fermionic neural networks pertaining to Wigner crystallization and the conservation of the symmetries of the many-body Hamiltonian, which is a *sine qua non* for exact many-body solutions.

[1] M. Jammer, *The Philosophy of Quantum Mechanics* (Wiley, New York, 1974).

[2] A. Pais, *Niels Bohr's Times: In Physics, Philosophy, and Polity* (Oxford University Press, Oxford, 1991).

[3] L. P. Kouwenhoven, C. M. Marcus, P. L. McEuen, S. Tarucha, R. M. Westervelt, and N. S. Wingreen, Electron transport in quantum dots, in *Mesoscopic Electron Transport*, edited by L. L. Sohn, L. P. Kouwenhoven, and G. Schön (Springer, Netherlands, Dordrecht, 1997), p. 105.

[4] R. Hanson, L. P. Kouwenhoven, J. R. Petta, S. Tarucha, and L. M. K. Vandersypen, Spins in few-electron quantum dots, Rev. Mod. Phys. **79**, 1217 (2007).

[5] F.-M. Jing, Z.-Z. Zhang, G.-Q. Qin, G. Luo, G. Cao, H.-O. Li, X.-X. Song, and G.-P. Guo, Gate-controlled quantum dots based on 2D materials, Adv. Quantum Technol. **5**, 2100162 (2022).

[6] F. A. Zwanenburg, A. S. Dzurak, A. Morello, M. Y. Simmons, L. C. L. Hollenberg, G. Klimeck, S. Rogge, S. N. Coppersmith, and M. A. Eriksson, Silicon quantum electronics, Rev. Mod. Phys. **85**, 961 (2013).

[7] L. M. K. Vandersypen and M. A. Eriksson, Quantum computing with semiconductor spins, Phys. Today **72**(8), 38 (2019).

[8] G.-W. Deng, N. Xu, and W.-J. Li, Gate-defined quantum dots: Fundamentals and applications, in *Quantum Dot Optoelectronic Devices*, edited by P. Yu and Z. M. Wang (Springer International Publishing, Cham, 2020), pp. 107–133.

[9] G. Burkard, T. D. Ladd, J. M. Nichol, A. Pan, and J. R. Petta, Semiconductor spin qubits, Rev. Mod. Phys. **95**, 025003 (2023).

[10] C. Yannouleas and U. Landman, Spontaneous Symmetry Breaking in Single and Molecular Quantum Dots, Phys. Rev. Lett. **82**, 5325 (1999).

[11] R. Egger, W. Häusler, C. H. Mak, and H. Grabert, Crossover from Fermi Liquid to Wigner Molecule Behavior in Quantum Dots, Phys. Rev. Lett. **82**, 3320 (1999).

[12] C. Yannouleas and U. Landman, Collective and Independent-Particle Motion in Two-Electron Artificial Atoms, Phys. Rev. Lett. **85**, 1726 (2000).

[13] A. V. Filinov, M. Bonitz, and Y. E. Lozovik, Wigner Crystallization in Mesoscopic 2D Electron Systems, Phys. Rev. Lett. **86**, 3851 (2001).

[14] C. Yannouleas and U. Landman, Strongly correlated wavefunctions for artificial atoms and molecules, J. Phys.: Condens. Matter **14**, L591 (2002).

[15] S. A. Mikhailov, Two ground-state modifications of quantum-dot beryllium, Phys. Rev. B **66**, 153313 (2002).

[16] A. Harju, S. Siljamäki, and R. M. Nieminen, Wigner molecules in quantum dots: A quantum Monte Carlo study, Phys. Rev. B **65**, 075309 (2002).

[17] C. Yannouleas and U. Landman, Two-dimensional quantum dots in high magnetic fields: Rotating-electron-molecule versus composite-fermion approach, Phys. Rev. B **68**, 035326 (2003).

[18] M. B. Tavernier, E. Anisimovas, F. M. Peeters, B. Szafran, J. Adamowski, and S. Bednarek, Four-electron quantum dot in a magnetic field, Phys. Rev. B **68**, 205305 (2003).

[19] C. Yannouleas and U. Landman, Structural properties of electrons in quantum dots in high magnetic fields: Crystalline character of cusp states and excitation spectra, Phys. Rev. B **70**, 235319 (2004).

[20] I. Romanovsky, C. Yannouleas, L. O. Baksmaty, and U. Landman, Bosonic Molecules in Rotating Traps, Phys. Rev. Lett. **97**, 090401 (2006).

[21] Y. Li, C. Yannouleas, and U. Landman, From a few to many electrons in quantum dots under strong magnetic fields: Properties of rotating electron molecules with multiple rings, Phys. Rev. B **73**, 075301 (2006).

[22] C. Yannouleas and U. Landman, Symmetry breaking and quantum correlations in finite systems: Studies of quantum dots and ultracold Bose gases and related nuclear and chemical methods, Rep. Prog. Phys. **70**, 2067 (2007).

[23] Z. Dai, J.-L. Zhu, N. Yang, and Y. Wang, Spin-dependent rotating Wigner molecules in quantum dots, Phys. Rev. B **76**, 085308 (2007).

[24] L. O. Baksmaty, C. Yannouleas, and U. Landman, Rapidly rotating boson molecules with long- or short-range repulsion: An exact diagonalization study, Phys. Rev. A **75**, 023620 (2007).

[25] A. Ghosal, A. D. Güçlü, C. J. Umrigar, D. Ullmo, and H. U. Baranger, Incipient Wigner localization in circular quantum dots, Phys. Rev. B **76**, 085341 (2007).

[26] N. Yang, J.-L. Zhu, and Z. Dai, Rotating Wigner molecules and spin-related behaviors in quantum rings, J. Phys.: Condens. Matter **20**, 295202 (2008).

[27] I. Romanovsky, C. Yannouleas, and U. Landman, Edge states in graphene quantum dots: Fractional quantum Hall effect analogies and differences at zero magnetic field, Phys. Rev. B **79**, 075311 (2009).

[28] B. B. Brandt, C. Yannouleas, and U. Landman, Double-well ultracold-fermions computational microscopy: Wave-function anatomy of attractive-pairing and Wigner-molecule entanglement and natural orbitals, Nano Lett. **15**, 7105 (2015).

[29] C. Yannouleas and U. Landman, Unified microscopic approach to the interplay of pinned-Wigner-solid and liquid behavior of the lowest Landau-level states in the neighborhood of $\nu = \frac{1}{3}$, Phys. Rev. B **84**, 165327 (2011); Fractional quantum Hall physics and higher-order momentum correlations in a few spinful fermionic contact-interacting ultracold atoms in rotating traps, Phys. Rev. A **102**, 043317 (2020); Exact closed-form analytic wave functions in two dimensions: Contact-interacting fermionic spinful ultracold atoms in a rapidly rotating trap, Phys. Rev. Res. **3**, L032028 (2021).

[30] H. E. Ercan, S. N. Coppersmith, and M. Friesen, Strong electron-electron interactions in Si/SiGe quantum dots, Phys. Rev. B **104**, 235302 (2021).

[31] J. C. Abadillo-Uriel, B. Martinez, M. Filippone, and Y.-M. Niquet, Two-body Wigner molecularization in asymmetric quantum dot spin qubits, Phys. Rev. B **104**, 195305 (2021).

[32] C. Yannouleas and U. Landman, Wigner molecules and hybrid qubits, J. Phys.: Condens. Matter **34**, 21LT01 (2022).

[33] C. Yannouleas and U. Landman, Molecular formations and spectra due to electron correlations in three-electron hybrid double-well qubits, Phys. Rev. B **105**, 205302 (2022).

[34] C. Ellenberger, T. Ihn, C. Yannouleas, U. Landman, K. Ensslin, D. Driscoll, and A. C. Gossard, Excitation Spectrum of Two Correlated Electrons in a Lateral Quantum Dot with Negligible Zeeman Splitting, Phys. Rev. Lett. **96**, 126806 (2006).

[35] S. Kalliakos, M. Rontani, V. Pellegrini, C. P. García, A. Pinczuk, G. Goldoni, E. Molinari, L. N. Pfeiffer, and K. W. West, A molecular state of correlated electrons in a quantum dot, Nat. Phys. **4**, 467 (2008).

[36] W. Jang, M.-K. Cho, H. Jang, J. Kim, J. Park, G. Kim, B. Kang, H. Jung, V. Umansky, and D. Kim, Single-shot readout of a driven hybrid qubit in a GaAs double quantum dot, Nano Lett. **21**, 4999 (2021).

[37] W. Jang, J. Kim, J. Park, G. Kim, M.-K. Cho, H. Jang, S. Sim, B. Kang, H. Jung, V. Umansky, and D. Kim, Wigner-molecularization-enabled dynamic nuclear field programming, Nat Commun **14**, 2948 (2023).

[38] J. Corrigan, J. P. Dodson, H. E. Ercan, J. C. Abadillo-Uriel, B. Thorgrimsson, T. J. Knapp, N. Holman, T. McJunkin, S. F. Neyens, E. R. MacQuarrie, R. H. Foote, L. F. Edge, M. Friesen, S. N. Coppersmith, and M. A. Eriksson, Coherent Control and Spectroscopy of a Semiconductor Quantum Dot Wigner Molecule, Phys. Rev. Lett. **127**, 127701 (2021).

[39] S. Pecker, F. Kuemmeth, A. Secchi, M. Rontani, D. C. Ralph, P. L. McEuen, and S. Ilani, Observation and spectroscopy of a two-electron Wigner molecule in an ultraclean carbon nanotube, Nat. Phys. **9**, 576 (2013).

[40] I. Shavitt, The history and evolution of configuration interaction, Mol. Phys. **94**, 3 (1998).

[41] C. Yannouleas and U. Landman, Electron and boson clusters in confined geometries: Symmetry breaking in quantum dots and harmonic traps, Proc. Natl. Acad. Sci. USA **103**, 10600 (2006).

[42] M. Rontani, C. Cavazzoni, D. Bellucci, and G. Goldoni, Full configuration interaction approach to the few-electron problem in artificial atoms, J. Chem. Phys. **124**, 124102 (2006).

[43] C. Yannouleas and U. Landman, Valleytronic full configuration-interaction approach: Application to the excitation spectra of Si double-dot qubits, Phys. Rev. B **106**, 195306 (2022).

[44] A. Szabo and N. S. Ostlund, *Modern Quantum Chemistry* (McGraw-Hill, New York, 1989), Chap. 4.

[45] V. N. Ostrovsky, What and how physics contributes to understanding the periodic law, Found. Chem. **3**, 145 (2001).

[46] J. Hubbard and B. H. Flowers, Electron correlations in narrow energy bands, Proc. R. Soc. London A **276**, 238 (1963).

[47] J. Hubbard, Generalized Wigner lattices in one dimension and some applications to tetracyanoquinodimethane (TCNQ) salts, Phys. Rev. B **17**, 494 (1978).

[48] S. Manzeli, D. Ovchinnikov, D. Pasquier, O. V. Yazyev, and A. Kis, 2D transition metal dichalcogenides, Nat. Rev. Mater. **2**, 17033 (2017).

[49] S. Carr, S. Fang, and E. Kaxiras, Electronic-structure methods for twisted moiré layers, Nat. Rev. Mater. **5**, 748 (2020).

[50] F. Wu, T. Lovorn, E. Tutuc, and A. H. MacDonald, Hubbard Model Physics in Transition Metal Dichalcogenide Moiré Bands, Phys. Rev. Lett. **121**, 026402 (2018).

[51] Y. Zhang, N. F. Q. Yuan, and L. Fu, Moiré quantum chemistry: Charge transfer in transition metal dichalcogenide superlattices, Phys. Rev. B **102**, 201115(R) (2020).

[52] M. Angeli and A. H. MacDonald, Γ-valley transition metal dichalcogenide moiré bands, Proc. Natl. Acad. Sci. USA **118**, e2021826118 (2021).

[53] Y. Pan, S. Fölsch, Y. Nie, D. Waters, Y.-C. Lin, B. Jariwala, K. Zhang, K. Cho, J. A. Robinson, and R. M. Feenstra, Quantum-confined electronic states arising from the moiré pattern of MoS_2-WSe_2 heterobilayers, Nano Lett. **18**, 1849 (2018).

[54] Y. Zeng and A. H. MacDonald, Strong modulation limit of excitons and trions in moiré materials, Phys. Rev. B **106**, 035115 (2022).

[55] Z. Song, Y. Wang, H. Zheng, P. Narang, and L.-W. Wang, Deep quantum-dot arrays in moiré superlattices of non-van der Waals materials, J. Am. Chem. Soc. **144**, 14657 (2022).

[56] T. Li, J. Zhu, Y. Tang, K. Watanabe, T. Taniguchi, V. Elser, J. Shan, and K. F. Mak, Charge-order-enhanced capacitance in semiconductor moiré superlattices, Nat. Nanotechnol. **16**, 1068 (2021).

[57] C. R. Kometter, J. Yu, T. Devakul, A. P. Reddy, Y. Zhang, B. A. Foutty, K. Watanabe, T. Taniguchi, and L. F. B. E. Feldman, Hofstadter states and reentrant charge order in a semiconductor moiré lattice, arXiv:2212.05068.

[58] Y. Li, C. Yannouleas, and U. Landman, Three-electron anisotropic quantum dots in variable magnetic fields: Exact results for excitation spectra, spin structures, and entanglement, Phys. Rev. B **76**, 245310 (2007).

[59] B. Szafran, F. M. Peeters, S. Bednarek, and J. Adamowski, Anisotropic quantum dots: Correspondence between quantum and classical Wigner molecules, parity symmetry, and broken-symmetry states, Phys. Rev. B **69**, 125344 (2004).

[60] Our findings concerning the prerequisites for WM pinning agree with the results in T. Chwiej and B. Szafran, Pinning of electron densities in quantum rings by defects: Symmetry constraints and distribution of persistent currents, Phys. Rev. B **79**, 085305 (2009).

[61] Y. Li, C. Yannouleas, and U. Landman, Artificial quantum-dot helium molecules: Electronic spectra, spin structures, and Heisenberg clusters, Phys. Rev. B **80**, 045326 (2009).

[62] See Supplemental Material at http://link.aps.org/supplemental/10.1103/PhysRevB.108.L121411 for more information concerning (1) The configuration interaction method. (2) The charge densities and the conditional probability distributions. (3) Additional charge densities and CPDs for $N = 4$ and $\phi = 10°$. (4) Additional charge densities for $N = 2-6$.

[63] I. Kimel and L. Elias, Relations between Hermite and Laguerre Gaussian modes, IEEE J. Quantum Electron. **29**, 2562 (1993).

[64] D. Xiao, G.-B. Liu, W. Feng, X. Xu, and W. Yao, Coupled Spin and Valley Physics in Monolayers of MoS_2 and Other Group-VI Dichalcogenides, Phys. Rev. Lett. **108**, 196802 (2012).

[65] N. Morales-Durán, P. Potasz, and A. H. MacDonald, Magnetism and quantum melting in moiré-material Wigner crystals, Phys. Rev. B **107**, 235131 (2023).

[66] Indeed, the term "rotating Wigner (or electron) molecule" has been used to accentuate the quantum nature of the Wigner molecule in earlier literature; see, e.g., Refs. [17,19,21–23,26].

[67] For the complete set of possible $N = 4$ spin eigenfunctions, see Ref. [61] and references therein.

[68] The subtle interplay discussed here between the *symmetry-preserving* exact CDs and the apparently *symmetry-breaking* intrinsic WM configurations has been noted and discussed in earlier literature; see Ref. [22] and references therein, Ref. [14], and J. A. Sheikh, J. Dobaczewski, P. Ring, L. M. Robledo, and C. Yannouleas, Symmetry restoration in mean-field approaches, J. Phys. G: Nucl. Part. Phys. **48**, 123001 (2021).

[69] For a comprehensive study of the dependence of the WM on ϕ (the strength of the trilobal anisotropy), see C. Yannouleas and U. Landman (unpublished).

[70] A similar degeneracy happens also for contact interaction; see C. Yannouleas, B. B. Brandt, and U. Landman, Ultracold few fermionic atoms in needle-shaped double wells: Spin chains and resonating spin clusters from microscopic Hamiltonians emulated via antiferromagnetic Heisenberg and t-J models, New J. Phys. **18**, 073018 (2016).

[71] L. P. Kouwenhoven, N. C. van der Vaart, A. T. Johnson, W. Kool, C. J. P. M. Harmans, J. G. Williamson, A. A. M. Staring, and C. T. Foxon, Single electron charging effects in semiconductor quantum dots, Z. Phys. B **85**, 367 (1991).

[72] The ν assignments in Ref. [56] correspond to $N - 1$ here.

[73] D. Wu, R. Rossi, F. Vicentini, N. Astrakhantsev, F. Becca, X. Cao, J. Carrasquilla, F. Ferrari, A. Georges, M. Hibat-Allah *et al.*, Variational benchmarks for quantum many-body problems, arXiv:2302.04919.

[74] H. Li, S. Li, E. C. Regan, D. Wang, W. Zhao, S. Kahn, K. Yumigeta, M. Blei, T. Taniguchi, K. Watanabe, S. Tongay, A. Zettl, M. F. Crommie, and F. Wang, Imaging two-dimensional generalized Wigner crystals, Nature (London) **597**, 650 (2021).

[75] E. Wach, D. P. Żebrowski, and B. Szafran, Charge density mapping of strongly-correlated few-electron two-dimensional quantum dots by the scanning probe technique, J. Phys.: Condens. Matter **25**, 335801 (2013).

[76] M. A. Topinka, B. J. LeRoy, S. E. J. Shaw, E. J. Heller, R. M. Westervelt, K. D. Maranowski, and A. C. Gossard, Imaging coherent electron flow from a quantum point contact, Science **289**, 2323 (2000).

[77] See version 2 of D. Luo, A. P. Reddy, T. Devakul, and L. Fu, Artificial intelligence for artificial materials: Moiré atom, arXiv:2303.08162.

[78] G. Cassella, H. Sutterud, S. Azadi, N. D. Drummond, D. Pfau, J. S. Spencer, and W. M. C. Foulkes, Discovering Quantum Phase Transitions with Fermionic Neural Networks, Phys. Rev. Lett. **130**, 036401 (2023).

SUPPLEMENTAL MATERIAL

Quantum Wigner molecules in moiré materials

Constantine Yannouleas and Uzi Landman

School of Physics, Georgia Institute of Technology, Atlanta, Georgia 30332-0430

(Dated: 19 April 2023)

THE CONFIGURATION INTERACTION METHOD

The full configuration interaction methodology has a long history, starting in quantum chemistry; see Refs. [1, 2]. The method was adapted to two dimensional problems and found extensive applications in the fields of semiconductor quantum dots [3–9] and of the fractional quantum Hall effect [10, 11].

Our 2D FCI is described in our earlier publications. The reader will find a comprehensive exposition in Appendix B of Ref. [8], where the method was applied to GaAs double-quantum-dot quantum computer qubits. The only difference with the present application to moiré QDs, due to the different external confinement, concerns the space orbitals, $\varphi_j(x, y)$, $j = 1, 2, \ldots, K$, that are employed in the building of the spin-dependent, single-particle basis used to construct the Slater determinants Ψ_I^N, which span the many-body Hilbert space [see Eq. (B4) in Ref. [8]; the index I counts the Slater determinants]. Indeed, for a moié QD, the orbitals $\varphi_j(x, y)$ are determined as solutions (in Cartesian coordinates) of the auxiliary Hamiltonian

$$H_{\text{aux}} = \frac{\mathbf{p}^2}{2m^*} + \frac{1}{2}m^*\omega_0^2(x^2 + y^2), \qquad (S1)$$

where $m^*\omega_0^2 = 16\pi^2 v_0 \cos(\phi)/a_M^2$, i.e., only the isotropic parabolic (harmonic) contribution in V_{MQD} is included.

Following Ref. [8], we use a sparse-matrix eigensolver based on Implicitly Restarted Arnoldi methods (see ARPACK [12]) to diagonalize the many-body Hamiltonian in Eq. (3) of the main text. When a finite magnetic field B value is used, we replace $\mathbf{p}$ by $\mathbf{p} - (e/c)\mathbf{A}(\mathbf{r})$, where the vector potential $\mathbf{A}(\mathbf{r}) = 0.5B(-y, x)$ is taken according to the symmetric gauge.

The required one-body and two-body matrix elements for the ARPACK diagonalization are calculated as described in Ref. [8]. In addition, the matrix elements $\langle\varphi_i(x, y)|\sin(3\theta)r^3|\varphi_j(x, y)\rangle$ of the anisotropic term in the moiré confinement are calculated analytically using the algebraic language MATHEMATICA [13] and the Hermite-to-Laguerre (Cartesian-to-polar) transformations listed in Ref. [14].

In all calculations, we used at a minimum values of $K = 45$ and/or $K = 55$. For $N = 2$ and $N = 3$, additional calculations were carried out employing an extended single-particle basis with $K = 78$. The maximum dimension of the many-body Hilbert space (the number of Slater determinants Ψ_I^N in the FCI expansion) reached a value of $I_{\text{max}} \approx 5,000,000$ in some cases.

CHARGE DENSITIES AND CONDITIONAL PROBABILITY DISTRIBUTIONS FROM FCI WAVE FUNCTIONS

The single-particle density (charge density) is the expectation value of a one-body operator

$$\rho(\mathbf{r}) = \langle\Phi_N^{\text{FCI}}|\sum_{i=1}^{N}\delta(\mathbf{r} - \mathbf{r}_i)|\Phi_N^{\text{FCI}}\rangle, \qquad (S2)$$

where Φ_N^{FCI} denotes the many-body (multi-determinantal) FCI wave function, namely,

$$\Phi_N^{\text{FCI}}(\mathbf{r}_1, \ldots, \mathbf{r}_N) = \sum_I C_I \Psi_I^N(\mathbf{r}_1, \ldots, \mathbf{r}_N). \qquad (S3)$$

Naturally several distinct spin structures can correspond to the same charge density. The spin structure associated with a specific FCI wave function can be determined with the help of the many-body spin-resolved CPDs [7, 10, 15–18].

The spin-resolved CPDs yield the conditional probability distribution of finding another fermion with up (or down) spin σ at a position $\mathbf{r}$, assuming that a given fermion with up (or down) spin σ_0 is fixed at $\mathbf{r_0}$. Specifically, the spin-resolved two-point anisotropic correlation function is defined as the the expectation value of a two-body operator

$$P_{\sigma\sigma_0}(\mathbf{r}, \mathbf{r}_0) = \langle\Phi_N^{\text{FCI}}|\sum_{i\neq j}\delta(\mathbf{r} - \mathbf{r}_i)\delta(\mathbf{r}_0 - \mathbf{r}_j)\delta_{\sigma\sigma_i}\delta_{\sigma_0\sigma_j}|\Phi_N^{\text{FCI}}\rangle. \qquad (S4)$$

Using a normalization constant

$$\mathcal{N}(\sigma, \sigma_0, \mathbf{r}_0) = \int P_{\sigma\sigma_0}(\mathbf{r}, \mathbf{r}_0)d\mathbf{r}, \qquad (S5)$$

we define a related conditional probability distribution (CPD) as

$$\mathcal{P}_{\sigma\sigma_0}(\mathbf{r}, \mathbf{r}_0) = P_{\sigma\sigma_0}(\mathbf{r}, \mathbf{r}_0)/\mathcal{N}(\sigma, \sigma_0, \mathbf{r}_0), \qquad (S6)$$

having the property $\int \mathcal{P}_{\sigma\sigma_0}(\mathbf{r}, \mathbf{r}_0)d\mathbf{r} = 1$.

ADDITIONAL CHARGE DENSITIES AND CPDs FOR $N = 4$ AND $\phi = 10°$

In Fig. SF1 (on p. III), we compare the charge densities for $N = 4$ at different values of the dielectric constant κ, i.e., $\kappa = 1000.00$, 10.0, 5.0, and 3.0. We further display for $N = 4$ the spin-resolved CPDs $\mathcal{P}_{\uparrow\downarrow}(\mathbf{r}, \mathbf{r}_0)$ and $\mathcal{P}_{\downarrow\downarrow}(\mathbf{r}, \mathbf{r}_0)$. In all frames, the value of the anisotropy control parameter is set to $\phi = 10°$. For $\kappa = 10$, corresponding to a weakened $e-e$ repulsion compared to that induced by the hBN environment ($\kappa = 5$), frames (e,f) provide further evidence of the unavoidability of WM formation in available TMD moiré materials.

ADDITIONAL CHARGE DENSITIES FOR $N = 2 - 6$

In this part, we present additional charge densities for parameters, different from those used in the main text; see Fig. SF2 (on p. IV) and Fig. SF3 (on p. V). In addition to the angle value of $\phi = 10°$, charge densities for the values of $\phi = 30°$ and $\phi = 0°$ are presented.

---

[1] I. Shavitt, The history and evolution of configuration interaction, Molecular Physics **94**, 3–17 (1998).

[2] A. Szabo and N. S. Ostlund, *Modern Quantum Chemistry* (McGraw-Hill, New York, 1989) For the Slater-Condon rules, see Chap. 4.

[3] C. Yannouleas and U. Landman, Two-dimensional quantum dots in high magnetic fields: Rotating-electron-molecule versus composite-fermion approach, Phys. Rev. B **68**, 035326 (2003).

[4] M. B. Tavernier, E. Anisimovas, F. M. Peeters, B. Szafran, J. Adamowski, and S. Bednarek, Four-electron quantum dot in a magnetic field, Phys. Rev. B **68**, 205305 (2003).

[5] M. Rontani, C. Cavazzoni, D. Bellucci, and G. Goldoni, Full configuration interaction approach to the few-electron problem in artificial atoms, The Journal of Chemical Physics **124**, 124102 (2006).

[6] Y. Li, C. Yannouleas, and U. Landman, Three-electron anisotropic quantum dots in variable magnetic fields: Exact results for excitation spectra, spin structures, and entanglement, Phys. Rev. B **76**, 245310 (2007).

[7] C. Yannouleas and U. Landman, Symmetry breaking and quantum correlations in finite systems: Studies of quantum dots and ultracold Bose gases and related nuclear and chemical methods, Reports on Progress in Physics **70**, 2067–2148 (2007).

[8] C. Yannouleas and U. Landman, Molecular formations and spectra due to electron correlations in three-electron hybrid double-well qubits, Phys. Rev. B **105**, 205302 (2022).

[9] C. Yannouleas and U. Landman, Valleytronic full configuration-interaction approach: Application to the excitation spectra of si double-dot qubits, Phys. Rev. B **106**, 195306 (2022).

[10] C. Yannouleas and U. Landman, Structural properties of electrons in quantum dots in high magnetic fields: Crystalline character of cusp states and excitation spectra, Phys. Rev. B **70**, 235319 (2004).

[11] J. K. Jain, *Composite Fermions* (Cambridge University Press, Cambridge, 2007).

[12] R. B. Lehoucq, D. C. Sorensen, and C. Yang, *ARPACK USERS' GUIDE: Solution of Large-Scale Eigenvalue Problems with Implicitly Restarted ARNOLDI Methods* (SIAM, Philadelphia, 1998).

[13] Wolfram Research, Inc., Mathematica, Version 13.2, Champaign, IL, 2022.

[14] I. Kimel and L. Elias, Relations between Hermite and Laguerre Gaussian modes, IEEE Journal of Quantum Electronics **29**, 2562–2567 (1993).

[15] C. Yannouleas and U. Landman, Collective and Independent-Particle Motion in Two-Electron Artificial Atoms, Phys. Rev. Lett. **85**, 1726–1729 (2000).

[16] Y. Li, C. Yannouleas, and U. Landman, From a few to many electrons in quantum dots under strong magnetic fields: Properties of rotating electron molecules with multiple rings, Phys. Rev. B **73**, 075301 (2006).

[17] Y. Li, C. Yannouleas, and U. Landman, Artificial quantum-dot Helium molecules: Electronic spectra, spin structures, and Heisenberg clusters, Phys. Rev. B **80**, 045326 (2009).

[18] B. B. Brandt, C. Yannouleas, and U. Landman, Double-well ultracold-fermions computational microscopy: Wave-function anatomy of attractive-pairing and Wigner-molecule entanglement and natural orbitals, Nano Letters **15**, 7105–7111 (2015).
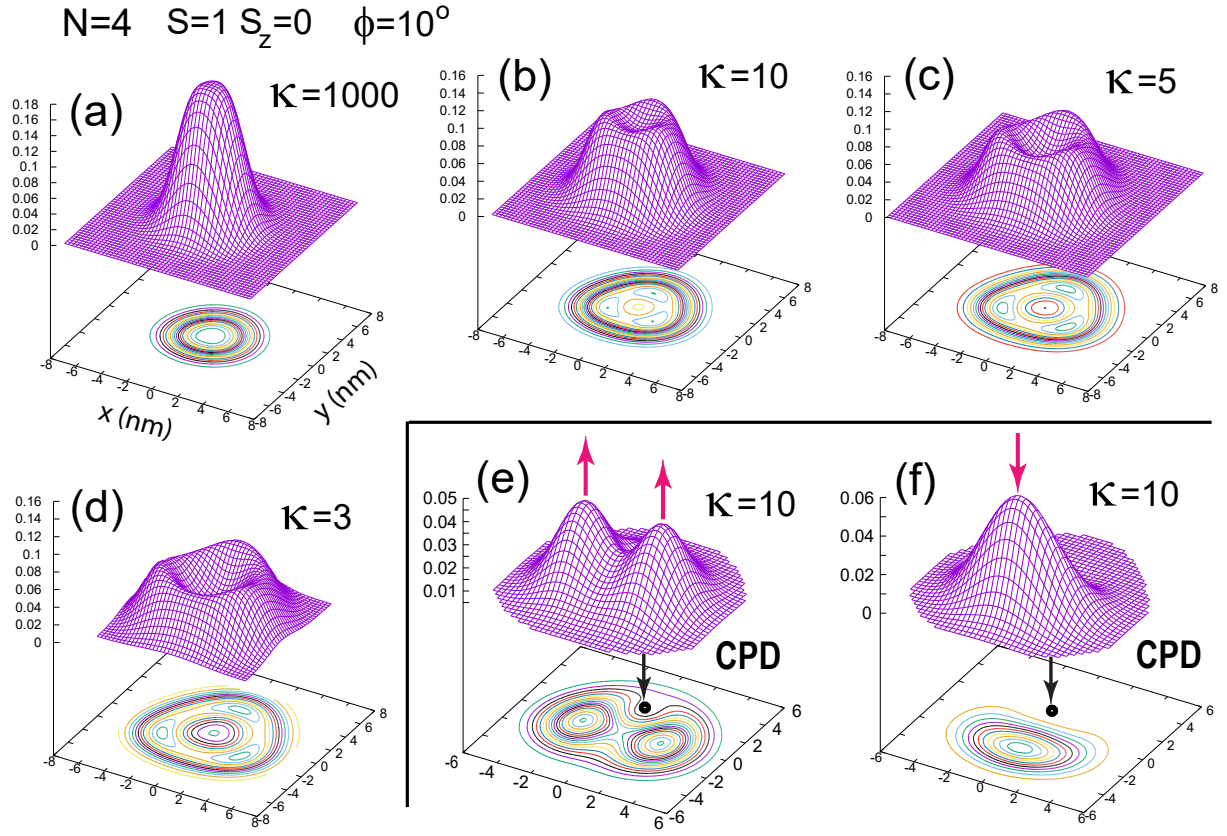
FIG. SF1. FCI moiré-QD charge densities for the total potential, V_{MQD}, [Eq. (2) of the main text] for $N = 4$ for various values of the dielectric constant $\kappa = 1000.00$ (a), 10.0 (b), 5.0 (c), and 3.0 (d). The (0,4) WM charge densities in frames (b), (c), and (d) contrast sharply with that of the non-interacting limit in frame (a). For $\kappa = 10$, corresponding to a weakened $e - e$ repulsion compared to that induced by the hBN environment ($\kappa = 5$), frames (e,f) provide further evidence of the unavoidability of WM formation in available TMD moiré materials. Remaining parameters: $S = 1$, $S_z = 0$, $m^* = 0.5 m_e$, $a_M = 14$ nm, $v_0 = 15$ meV, and $\phi = 10°$.
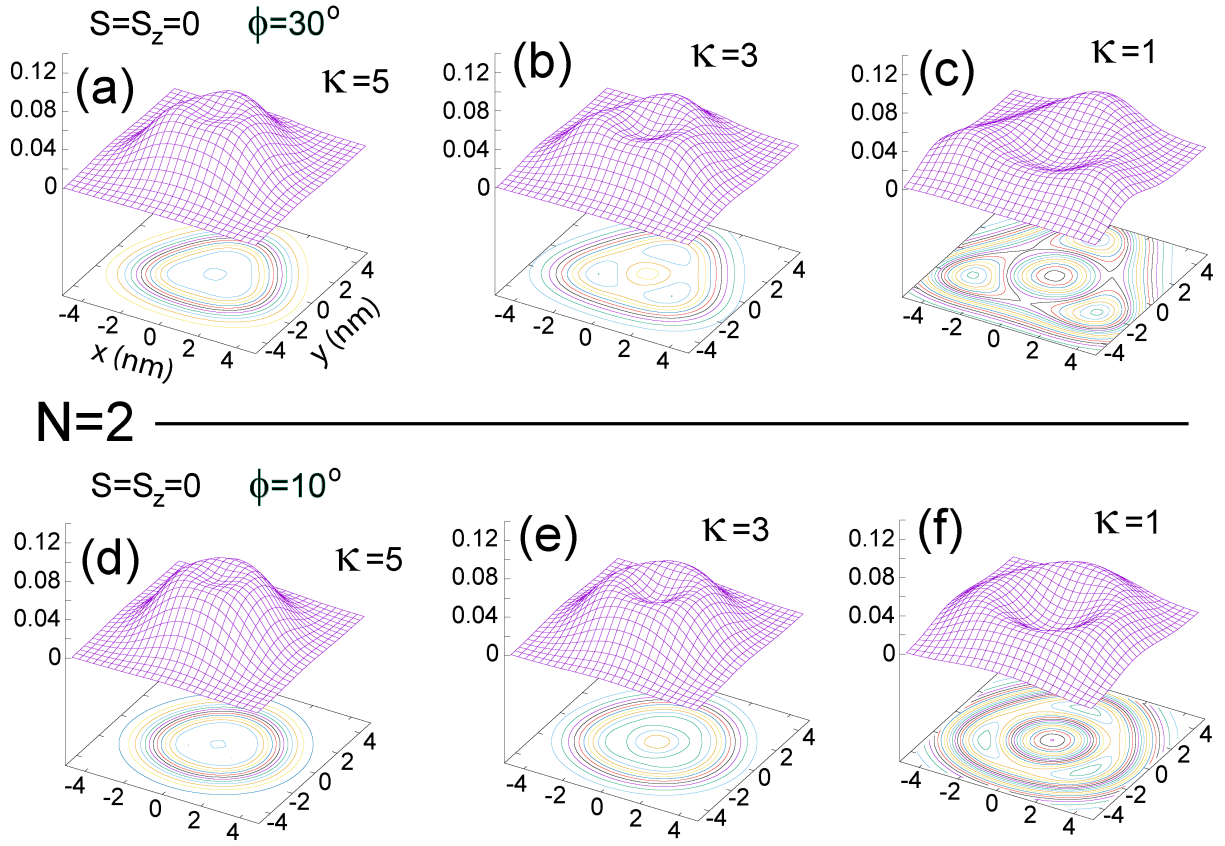
FIG. SF2. FCI moiré-QD charge densities [i.e., for the total potential, V_{MQD}, in Eq. (2) of the main text which includes both the harmonic and cubic contributions] for the singlet state of $N = 2$ holes, and for different values of the dielectric constant κ and the angle ϕ. Remaining parameters used: $a_M = 14$ nm, $v_0 = 15$ meV, $m^* = 0.5m_e$. (a-c) $\phi = 30°$. (d-f) $\phi = 10°$. Left column: $\kappa = 5$. Middle column: $\kappa = 3$. Right column: $\kappa = 1$. The corresponding Wigner parameter (R_W) values are: (a) 3.69, (b) 6.15, (c) 18.46, (d) 3.57, (e) 5.95, and (f) 17.85. The progressive enhancement of the depression at the origin as a function of decreasing κ (increasing R_W) is clearly seen for the cases of both angles ϕ. These ring-like charge densities correspond to a rotating Wigner molecule whose intrinsic geometric configuration [denoted by (0,2)] consists of two antipodal fermions; see main text. CDs in units of $1/nm^2$.

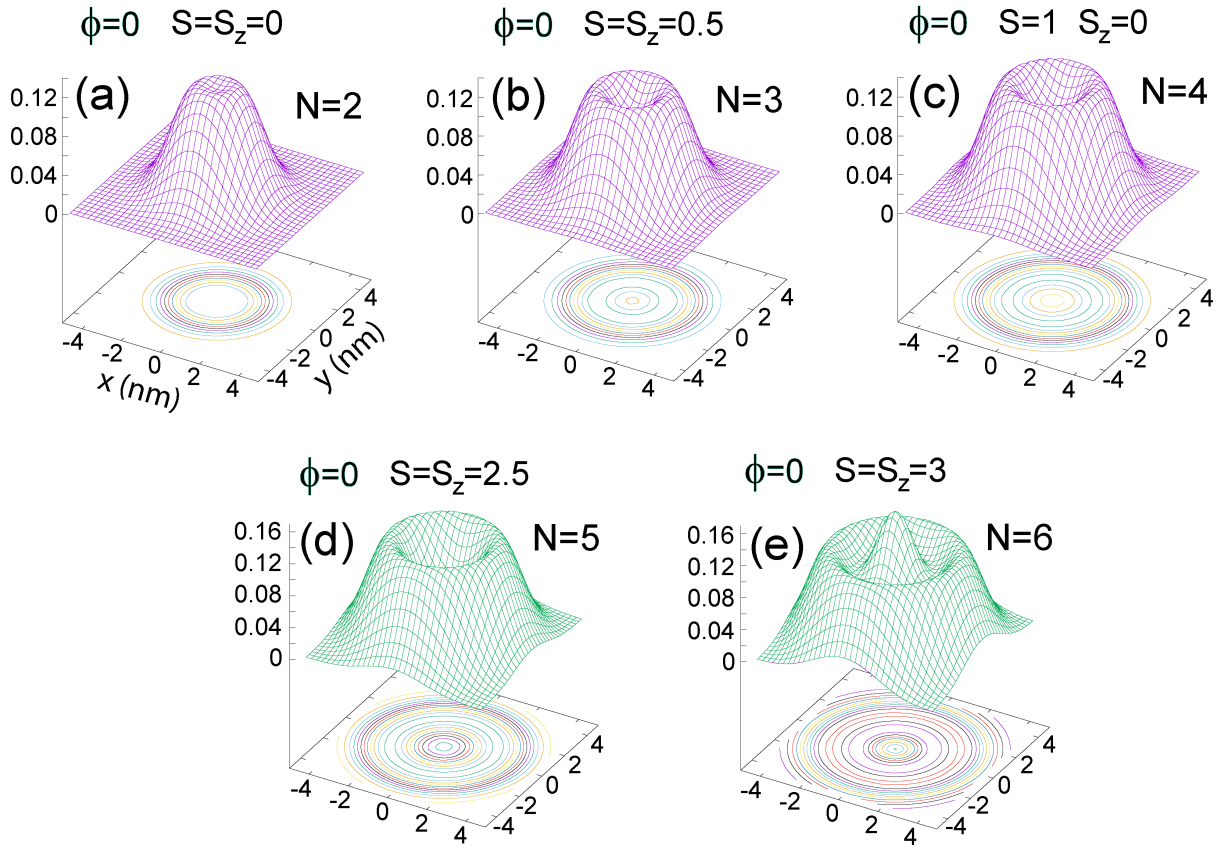FIG. SF3. FCI moiré-QD, charge densities for the total potential, V_{MQD}, [Eq. (2) of the main text] for a vanishing angle $\phi = 0°$. In this case only the harmonic term in the expansion survives, and the confinement has circular symmetry. (a) ground-state CD for $N = 2$ holes. (b) ground-state CD for $N = 3$ holes. (c) ground-state CD for $N = 4$ holes. (d,e) CDs of the lowest-in-energy fully spin-polarized states for $N = 5$ and $N = 6$ holes, respectively. The remaining parameters are: $a_M = 15$ nm, $v_0 = 20$ meV, $m^* = 1\ m_e$, and $\kappa = 10$, which yields $R_W = 2.88$. These uniform, ring-like charge densities correspond to a rotating Wigner molecule whose intrinsic geometric configuration [denoted as $(0, N)$ or $(1, N-1)$] consists of regular polygons with the particles being localized at the apices of the polygons. The results in this figure are in full agreement with the previous abundant literature on 2D semiconductor quantum dots; see Ref. [7] and references therein. CDs in units of $1/nm^2$.